LETTERS
PUBLISHED ONLINE: 10 NOVEMBER 2014 | DOI: 10.1038/NNANO.2014.252
nature nanotechnology

Magnonic charge pumping via spin–orbit coupling

Chiara Ciccarelli[1‡], Kjetil M. D. Hals[2,3‡], Andrew Irvine[1], Vit Novak[4], Yaroslav Tserkovnyak[5], Hidekazu Kurebayashi[1,6†], Arne Brataas[2*] and Andrew Ferguson[1]

The interplay between spin, charge and orbital degrees of freedom has led to the development of spintronic devices such as spin-torque oscillators and spin-transfer torque magnetic random-access memories. In this development, spin pumping represents a convenient way to electrically detect magnetization dynamics[1–6]. The effect originates from direct conversion of low-energy quantized spin waves in the magnet, known as magnons, into a flow of spins from the precessing magnet to adjacent leads. In this case, a secondary spin–charge conversion element, such as heavy metals with large spin Hall angle[4–6] or multilayer layouts[7], is required to convert the spin current into a charge signal. Here, we report the experimental observation of charge pumping in which a precessing ferromagnet pumps a charge current, demonstrating direct conversion of magnons into high-frequency currents via the relativistic spin–orbit interaction. The generated electric current, unlike spin currents generated by spin-pumping, can be directly detected without the need of any additional spin–charge conversion mechanism. The charge-pumping phenomenon is generic and gives a deeper understanding of its reciprocal effect, the spin orbit torque, which is currently attracting interest for their potential in manipulating magnetic information.

A flow of spin angular momentum without an accompanying charge current is called a pure spin current. A simple way to generate pure spin currents is via spin-pumping[8]. The phenomenon originates from direct conversion of low-energy quantized spin-waves in the magnet, known as magnons, into a flow of spins from the precessing magnet to adjacent normal metal leads. The reciprocal effect, in which a spin current is able to excite magnetization dynamics, is known as the spin-transfer torque. In this case, spin-angular momentum is transferred from the carriers to the magnet, applying a torque to the magnetization[9]. This pair of reciprocal effects underlies much of the progress in spintronics to date.

Spin–orbit coupling provides an efficient route to the electrical generation of magnetic torques from orbital motion, that is, from an electric current (Fig. 1a,c)[10–17]. These relativistic spin–orbit torques (SOTs) exist in ferromagnets with broken spatial inversion symmetry. They have been reported in (Ga,Mn)As, a material with a broken bulk inversion symmetry[18–21], as well as in heterostructures comprising ferromagnetic metals[22–27]. The SOT has been observed to have both field-like[18,22] and damping-like[21,24,25] contributions. Unlike spin-transfer torques, SOTs do not rely on a secondary element that spin-polarizes the currents; instead, a spin-polarization results from the carrier velocity. Despite showing promise for magnetic memory applications, the understanding of SOTs remains immature, and further development of the field requires improved theoretical models and experimental techniques to reveal their full complexity. The Onsager reciprocity relations[28] imply that, as for spin-pumping/spin-transfer torque, there is a reciprocal phenomenon for the SOT, namely, charge pumping generated from magnetization precession (Fig. 1b,d)[14,29].

The underlying physics of charge pumping is direct conversion of magnons into charge currents via spin–orbit coupling. We will therefore refer to this process as 'magnonic charge pumping'. Any external force that drives magnetization precession can generate magnonic charge pumping. Examples of potential driving forces include magnetic fields, alternating currents, thermal gradients or circularly polarized light pulses. Magnonic charge pumping can be a favourable alternative to spin pumping for the detection of magnetization dynamics, because the effect does not require an additional conversion mechanism to be measureable. Moreover, charge pumping contains information about the SOTs and therefore opens the door for a novel experimental technique to explore these relativistic torques. Because the coefficients that describe the SOT are related to those that describe charge pumping, via the Onsager relations, it is possible to experimentally measure the amplitude and symmetry of the spin–orbit torque to determine the expected charge-pumping signal. In our experiment, we do this and compare the result to the experimentally measured charge-pumping signal.

A simple explanation of magnonic charge pumping can be found from the Hamiltonian

$$H = \mathbf{p}^2/2m + \mathbf{p}\cdot\boldsymbol{\Lambda}\cdot\boldsymbol{\sigma} + \Delta\mathbf{m}\cdot\boldsymbol{\sigma} \quad (1)$$

where $\boldsymbol{\sigma} = (\sigma_1, \sigma_2, \sigma_3)$ is the carrier's spin operator represented by the Pauli matrices $\boldsymbol{\sigma}_i$, $\mathbf{p}$ is the momentum operator, Δ is the exchange splitting and $\mathbf{m}$ is the unit vector in the direction of magnetization. The second term in Hamiltonian (1) represents spin–orbit coupling, where matrix $\boldsymbol{\Lambda}$ parameterizes this coupling. The velocity operator resulting from Hamiltonian (1) is

$$\mathbf{v} = \partial H/\partial\mathbf{p} = \mathbf{p}/m + \boldsymbol{\Lambda}\cdot\boldsymbol{\sigma} \quad (2)$$

The last term in equation (2) is the anomalous term, which mediates a coupling between spin and momentum. In ferromagnets, excitations of magnons result in a net non-equilibrium spin accumulation $\delta\langle\boldsymbol{\sigma}\rangle(t)$ due to the exchange interaction, yielding an average velocity response $\delta\langle\mathbf{v}\rangle(t) = \boldsymbol{\Lambda}\cdot\delta\langle\boldsymbol{\sigma}\rangle(t)$ that produces an alternating current density $\mathbf{j} \approx \boldsymbol{\Lambda}\cdot\delta\langle\boldsymbol{\sigma}\rangle(t)$. Because the magnon frequencies are low compared to the exchange splitting, the spin-density response is proportional to the rate of change $\partial\mathbf{m}/\partial t$ of the magnetization, that is, $\delta\langle\boldsymbol{\sigma}\rangle(t) \approx \partial\mathbf{m}/\partial t$. Consequently, the induced current density is also proportional to $\partial\mathbf{m}/\partial t$, where the coefficient of

[1]Cavendish Laboratory, University of Cambridge, Cambridge CB3 0HE, UK, [2]Department of Physics, Norwegian University of Science and Technology, NO-7491, Trondheim, Norway, [3]Niels Bohr International Academy and the Center for Quantum Devices, Niels Bohr Institute, University of Copenhagen, 2100 Copenhagen, Denmark, [4]Institute of Physics ASCR, v.v.i., Cukrovarnická 10, 162 53 Praha 6, Czech Republic, [5]Department of Physics and Astronomy, University of California, Los Angeles, California 90095, USA, [6]PRESTO, Japan Science and Technology Agency, Kawaguchi 332-0012, Japan; †Present address: London Centre for Nanotechnology, University College London, London WC1H 0AH, UK and Department of Electronic and Electrical Engineering, University College London, London WC1E 7JE, UK; ‡These authors contributed equally to this work. *e-mail: arne.brataas@ntnu.no

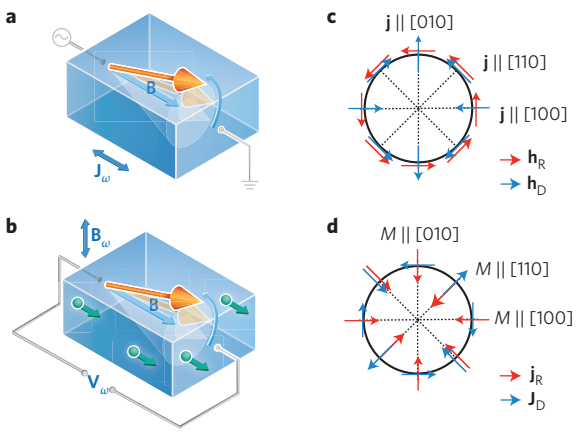

Figure 1 | Spin–orbit torque and charge pumping. a, A charge current through (Ga,Mn)As results in a non-equilibrium spin polarization of the carriers, which exchange-couples to the magnetization and exerts a torque. The effect is induced by spin–orbit coupling, which mediates the transfer of orbital momentum to spin angular momentum. An alternating current generates a time-varying torque, which drives magnetic precession resonantly when a magnetic field is applied. **b**, The reciprocal effect of **a**. Magnetization precession leads to a non-equilibrium spin concentration, which pumps charge (green arrows) and is converted into an alternating charge current by the spin–orbit coupling. **c**, Polar plot illustrating the direction of the effective magnetic field induced by a charge current along different crystal directions. The Rashba ($\mathbf{h}_R$) and Dresselhaus ($\mathbf{h}_D$) spin–orbit coupling contributions are indicated by red and blue arrows, respectively. **d**, Polar plot illustrating the direction of the charge current pumped by magnetization precession around different crystal directions. The Rashba ($\mathbf{j}_R$) and Dresselhaus ($\mathbf{j}_D$) contributions are indicated by red and blue arrows, respectively.

proportionality is directly related to the spin–orbit coupling matrix, $\mathbf{j} \approx \mathbf{\Lambda} \cdot \partial \mathbf{m}/\partial t$.

We chose compressively strained (Ga,Mn)As on GaAs as the material with which to demonstrate magnonic charge pumping. (Ga,Mn)As is indeed characterized by crystal inversion asymmetry, which together with strain leads to easily identifiable SOTs with both Rashba and Dresselhaus symmetry[30]. Furthermore, the use of (Ga,Mn)As avoids the complexity associated with a competing torque originating in the spin Hall effect, which is present in layered metal systems[20,31]. The symmetry of strained (Ga,Mn)As is described by the crystallographic point group C_{2v}, where the two-fold symmetry axis is perpendicular to the epilayer[30]. In the frame of reference where x' is along crystallographic direction [110], z' is along the two-fold symmetry axis and y' is perpendicular to x' and z', $\mathbf{\Lambda} \approx i\boldsymbol{\sigma}_2$ and $\mathbf{\Lambda} \approx \boldsymbol{\sigma}_1$ parameterize the Rashba and Dresselhaus spin–orbit coupling, respectively, and the induced alternating current density is given by

$$\mathbf{j}^{(r)} = \Lambda_D^{(r)} \boldsymbol{\sigma}_1 \cdot \partial \mathbf{m}_{\|}/\partial t - i\Lambda_R^{(r)} \boldsymbol{\sigma}_2 \cdot \partial \mathbf{m}_{\|}/\partial t \quad (3)$$

Here, $\mathbf{m}_{\|} = (m_{x'}, m_{y'})$ denotes the in-plane component of the magnetization, and parameters $\Lambda_R^{(r)}$ and $\Lambda_D^{(r)}$ characterize the strength of the charge current pumped magnonically via the Rashba and Dresselhaus spin–orbit coupling, respectively. The current density in equation (3) is reciprocal to the field-like SOT, $\boldsymbol{\tau} \approx \mathbf{m} \times \mathbf{h}^{so}$, where $\mathbf{h}^{so}$ is the effective SOT field induced by an applied current density $\mathbf{J}$. The SOT field consists of terms with Rashba and Dresselhaus symmetry, that is, $\mathbf{h}^{so} = h_D \boldsymbol{\sigma}_1 \cdot \mathbf{J}_{\|} + i h_R \boldsymbol{\sigma}_2 \cdot \mathbf{J}_{\|}$, where parameters h_R and h_D are linked via the reciprocity relations to $\Lambda_R^{(r)}$ and $\Lambda_D^{(r)}$, respectively.

The terms in equation (3) represent reactive charge-pumping processes because they are even under time reversal. In addition, there are dissipative contributions to the magnonic charge pumping, which are related via the reciprocity relations to the anti-damping SOT. The in-plane component of the dissipative current is given by

$$\mathbf{j}^{(d)} = \Lambda_R^{(d)} \mathbf{m}_{\|} \partial m_{z'}/\partial t + \Lambda_D^{(d)} \boldsymbol{\sigma}_3 \cdot \mathbf{m}_{\|} \partial m_{z'}/\partial t \quad (4)$$

where the phenomenological parameters $\Lambda_R^{(d)}$ and $\Lambda_D^{(d)}$ characterize dissipative charge pumping by Rashba and Dresselhaus spin–orbit coupling, respectively (see Supplementary Section 1E for a detailed derivation).

When the magnetization precesses with frequency ω_0 and amplitude A, there is a reactive contribution to the pumped current oscillating at the same frequency with an amplitude of $j_\omega^{(r)} = A\omega_0 \Lambda_{R,D}^{(r)}$. The polar plot in Fig. 1d shows the symmetry of the Rashba and Dresselhaus contributions to the pumped current for different magnetization directions. Figure 1c illustrates the symmetry of the reciprocal effect and shows the direction of the reactive components of the Rashba and Dresselhaus SOT fields for different directions of the applied current. There is also a direct current induced by the magnetization precession (Supplementary Section 1F). However, its value is small because it is second order in the precession amplitude and proportional to the Gilbert damping constant α_G, so it will not be discussed further.

Figure 2a presents a schematic of the measuring apparatus. Overall, the experiment involves a microwave current density passed through the bar and three magnetic fields: one generated by the microwave current (the SO field $\mu_0 h_{so}$), a modulation field B_{mod} and a static magnetic field B. Magnetization precession is excited by $\mu_0 h_{so}$ in a microbar patterned from an epilayer with a nominal 9% Mn concentration. During magnetization precession, frequency mixing between the alternating current and the oscillating magneto-resistance leads to a time-independent voltage V_{dc} (ref. 20). Using V_{dc}, we experimentally determined the components of the SOT, introducing a rotated reference frame where x is along the bar (current) direction and z is perpendicular to the epilayer (Fig. 2). Angle θ refers to the mean position of the magnetization in the x–y plane and is measured from the x-axis. We focused our experiments on the two bar directions [100] and [010], because the SOT field components h_{so}^x and h_{so}^y then originate purely from the field-like SOTs, which have symmetries that resemble, respectively, the Dresselhaus and Rashba spin–orbit interactions (Fig. 1c). Figure 2b shows the derivative of the rectified voltage $(dV_{dc}/dB)B_{mod}$, measured with a field modulation lock-in technique, for a bar oriented along the [100] direction when the in-plane magnetic field B is swept through the ferromagnetic resonance condition. The position of the resonance as a function of the field direction follows the modified Kittel's formula for an in-plane magnetized material with an additional uniaxial anisotropy[32]. The SOT-field $\mathbf{h}_{so}$ can be directly extracted from the angle dependence of the antisymmetric and symmetric parts of the resonance, and the coefficients are summarized in Table 1. The SOT field components h_{so}^x and h_{so}^y correspond to the coefficients h_D and h_R introduced earlier, while the angle-dependent h_{so}^z terms represent the antidamping contribution. In accordance with a trend that we have observed previously, the present material has a weaker SOT than in the case with lower Mn concentration[20].

In the second part of the experiment we measured magnonic charge pumping. When magnetization precession is excited by $\mu_0 h_{so}$, an alternating voltage V_ω at the same frequency of precession is induced by charge pumping across the bar, which thus behaves as a voltage source. The generated signal V_ω is transmitted through the lines and measured with a homodyne detection technique (Supplementary section 'Experimental set-up' gives more details on the measurement circuitry). Figure 2c presents the

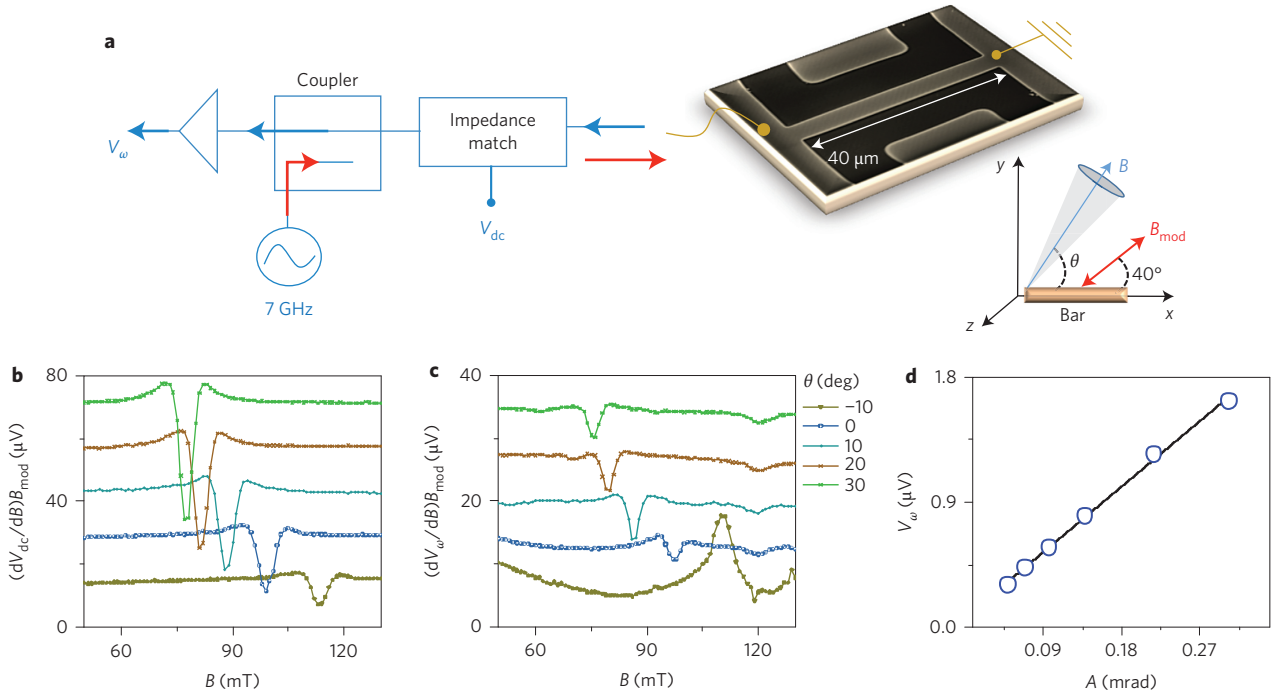

Figure 2 | Charge-pumping experiment. a, Schematics of the measuring set-up. A 7 GHz microwave signal (red arrow) is launched towards a (Ga,Mn)As bar via an impedance-matching circuit. The microwave current passed through the bar excites magnetization precession via SOT when an in-plane magnetic field **B** is swept through the resonance. The orientation of the field is defined with respect to the bar direction, as shown on the Cartesian plot. The microwave voltage generated in (Ga,Mn)As by magnonic charge pumping (blue arrow) is transmitted through the same impedance matcher to the microwave circuitry, where the amplitude of the signal is amplified and detected. A low-frequency lock-in field-modulation technique is used, with a 3.3 mT oscillating magnetic field B_{mod} applied at 45° from the bar direction. A directional coupler separates the incoming signal used to excite magnetic precession from the outgoing signal generated both by magnonic charge pumping and the microwave signal reflected from the circuit. The impedance-matching circuit also includes a bias tee that allows the rectified voltage along the bar to be measured. **b**, Derivative of the rectified voltage along the a [100]-oriented bar, $(dV_{dc}/dB)B_{mod}$, measured by a field-modulation lock-in technique as the magnetic field is swept along different in-plane directions. **c**, Derivative of the microwave voltage along a [100]-oriented bar, $(dV_\omega/dB)B_{mod}$, induced by magnonic charge pumping for the same field directions as in **b**. **d**, Amplitude of microwave voltage V_ω as a function of precessional amplitude A. The value of A (in mrad) is obtained from the amplitude of the rectified voltage $|V_{dc}| = |I| R_{AMR}A/2$, where I is the microwave current passing through the bar and R_{AMR} is the anisotropic magneto-resistance coefficient.

derivative of the amplitude of the microwave voltage across the sample, $(dV_\omega/dB)B_{mod}$, as the magnetic field is swept along different in-plane directions. At ferromagnetic resonance, a resonance also appears in V_ω, which indicates that a microwave electrical signal is generated within the sample by the precessing magnetization.

Magnonic charge pumping is proportional to the rate of change of magnetization, so the induced microwave amplitude should be linearly dependent on the precessional amplitude. To check this characteristic we measured voltage V_ω as a function of the precessional amplitude A for a fixed direction of the magnetic field. The amplitude was controlled by the value of the applied microwave current. Figure 2d clearly demonstrates a linear dependence on the amplitude. This excludes the possibility that V_ω originates from mixing between the microwave current and the modulated resistance during precession, because such higher-order terms depend nonlinearly on the amplitude (see Supplementary Information).

Table 1 | Coefficients of SOT measured for samples with current along the [100] and [010] directions, normalized to a current density of 1×10^6 A cm^{-2}.

	$\mu_0 h^x_{so}$	$\mu_0 h^y_{so}$	$\mu_0 h^z_{so}$ sinθ term	$\mu_0 h^z_{so}$ cosθ term
[100]	−6.1	−8.7	8.5	−13.6
[010]	5.2	−5.5	−5.5	−6.9

All values are in µT. The first-order (sinθ and cosθ) harmonic components of h^z_{so} are extracted from fits to the experimental data.

Next, we demonstrate that the measured signal is reciprocal to the SOT. To this end, we modelled charge pumping using equations (3) and (4) (see Supplementary Section 1E for further details). Using the Onsager reciprocity relations, the measured SOT fields h^y_{so} and h^x_{so} determine the values of $\Lambda^{(r)}_R$ and $\Lambda^{(r)}_D$, respectively, while the measured h^z_{so} component determines $\Lambda^{(d)}_R$ and $\Lambda^{(d)}_D$. The expression for $\partial\mathbf{m}/\partial t$ is found from the solution of the Landau–Lifshitz–Gilbert (LLG) equation. The resulting voltage signal across the bar is given by the total current pumped along the bar direction multiplied by the resistance. Figure 3a,b presents the magnitude of the symmetric and antisymmetric components of the integrated resonances with respect to the field direction. The theoretical curves are represented by continuous lines and show agreement with the experimental data in both symmetry and amplitude. This verifies that the measured voltage signal satisfies its reciprocal relationship to the SOT. The different symmetries found for the [100] and [010] bar directions further confirm the crystal, and therefore SOC-related origin of the effect, and exclude the Oersted field and artefacts in the measuring set-up as possible origins. Also, a variation of the impedance matching following the a.c. change in magnetic susceptibility during precession cannot justify the resonance in V_ω, as in this case the symmetry would be dominated by the symmetry of the anisotropic magneto-resistance (see Supplementary Information). The slight discrepancy between the experimental and theoretical curves arises from higher-order

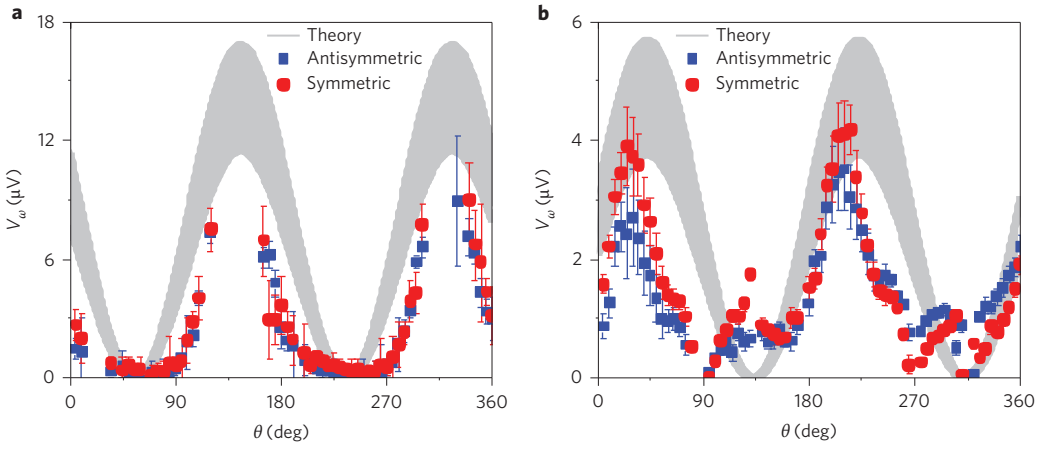

Figure 3 | Theoretical modelling of measured angular dependence of charge pumping. Symmetric and antisymmetric components of the integrated resonances shown in Fig. 2c for different directions of external field **B**. **a**,**b**, Results obtained for a bar oriented along the [100] crystal direction (**a**) and for a bar oriented along the [010] direction (**b**). Data are compared to the theoretical band calculated without any fitting parameters from the values of the SO field components, by including the error (symmetric and antisymmetric contributions are equal and are shown by a unique band). For a more detailed discussion of the theoretical model and the error see Supplementary Information.

harmonics in the phenomenological expansion of the pumped current. Such higher-order features have also been observed in the SOT[25]. To allow comparison of the magnonic charge pumping between different materials, we renormalized the pumped current density with the saturation magnetization, frequency and precessional amplitude. For our (Ga,Mn)As samples we found a magnitude of 600 μA cm^{-2}/T GHz for the [100] direction and 240 μA cm^{-2}/T GHz for the [010] direction. In ref. 20, the authors reported fluctuations of 30% in the magnitude of the SOT for samples of the same material. Similarly, the magnitude of the charge pumping is expected to be sample-dependent, although its symmetry is only determined by the crystalline orientation of the bar, as also shown in Supplementary Section 1E.

In conclusion, we have demonstrated direct conversion of magnons into high-frequency currents via spin–orbit coupling. Although we chose the ferromagnetic semiconductor (Ga,Mn)As, magnonic charge pumping is also predicted in layered systems like Pt/Co/Al_2O_3 and can be quantitatively analysed within the same Onsager framework provide here. In these metallic systems, we expect a large, room-temperature charge-pumping effect, the investigation of which will help distinguish between spin Hall and spin–orbit torques.

Methods and materials

Materials. The 18-nm-thick ($Ga_{0.91}$,$Mn_{0.09}$)As epilayer was grown on a GaAs [001] substrate by molecular beam epitaxy. It was subsequently annealed for 8 h at 200 °C. It had a Curie temperature of 179 K, a room-temperature conductivity of 414 Ω^{-1} cm^{-1}, which increased to 544 Ω^{-1} cm^{-1} at 4 K, and a saturation magnetization of 70.8 e.m.u. cm^{-3}.

Devices. Two terminal microbars were patterned in different crystal directions by electron-beam lithography and had dimensions of 4 μm × 40 μm.

Experimental procedure. A 7 GHz microwave signal with a source power of 18 dBm was transmitted to an impedance-matching circuit comprising a four-finger interdigitated capacitor and a λ/2 microstrip resonator patterned on a low-loss printed circuit board and reached the (Ga,Mn)As bar, which was wire-bonded between the resonator and the ground plane. SOT excited magnetic precession as an external field was swept in the plane of the device. The microwave voltage generated in the (Ga,Mn)As bar by magnonic charge pumping was transmitted via a directional coupler to an amplifier and mixer, from which we measured the amplitude of the voltage. Low-frequency (222 Hz) field modulation with an amplitude of 3.3 mT was adopted, together with lock-in detection, to remove the charge-pumping signal from the reflected microwave signal. When driven at its fundamental frequency (7 GHz), there was a node of electric field at the centre point of the resonator, and it was possible to incorporate a bias-tee by simple wire-bonding. This allowed the rectification voltage across the bar to be measured. All measurements were performed at a temperature of 30 K.

Received 1 July 2014; accepted 1 October 2014; published online 10 November 2014

References

1. Mizukami, S., Ando, Y. & Miyazaki, T. The study on ferromagnetic resonance linewidth for NM/80NiFe/NM (NM = Cu, Ta, Pd and Pt) films. *Jpn. J. Appl. Phys.* **40,** 580–585 (2001).
2. Heinrich, B. *et al.* Dynamic exchange coupling in magnetic bilayers. *Phys. Rev. Lett.* **90,** 187601 (2003).
3. Costache, M. V., Sladkov, M., Watts, S. M., van der Wal, C. H. & van Wees, B. J. Electrical detection of spin pumping due to the precessing magnetization of a single ferromagnet. *Phys. Rev. Lett.* **97,** 216603 (2006).
4. Mosendz, O. *et al.* Quantifying spin Hall angles from spin pumping: experiments and theory. *Phys. Rev. Lett.* **104,** 046601 (2010).
5. Kajiwara, Y. *et al.* Transmission of electrical signals by spin–wave interconversion in a magnetic insulator. *Nature* **464,** 262–267 (2010).
6. Sandweg, C. W. *et al.* Spin pumping by parametrically excited exchange magnons. *Phys. Rev. Lett.* **106,** 216601 (2011).
7. Sánchez, J. C. R. *et al.* Spin-to-charge conversion using Rashba coupling at the interface between non-magnetic materials. *Nature Commun.* **4,** 2944 (2013).
8. Tserkovnyak, Y., Brataas, A., Bauer, G. E. W. & Halperin, B. I. Nonlocal magnetization dynamics in ferromagnetic heterostructures. *Rev. Mod. Phys.* **77,** 1375–1421 (2005).
9. Ralph, D. C. & Stiles, M. D. Spin transfer torques. *J. Magn. Magn. Mater.* **320,** 1190–1216 (2008).
10. Bernevig, B. A. & Vafek, O. Piezo-magnetoelectric effects in p-doped semiconductors. *Phys. Rev. B* **72,** 033203 (2005).
11. Manchon, A. & Zhang, S. Theory of nonequilibrium intrinsic spin torque in a single nanomagnet. *Phys. Rev. B* **78,** 212405 (2008).
12. Manchon, A. & Zhang, S. Theory of spin torque due to spin–orbit coupling. *Phys. Rev. B* **79,** 094422 (2009).
13. Garate, I. & MacDonald, A. H. Influence of a transport current on magnetic anisotropy in gyrotropic ferromagnets. *Phys. Rev. B* **80,** 134403 (2009).
14. Hals, K. M. D., Brataas, A. & Tserkovnyak, Y. Scattering theory of charge-current-induced magnetization dynamics. *Europhys. Lett.* **90,** 47002 (2010).
15. Pesin, D. A. & MacDonald, A. H. Quantum kinetic theory of current-induced torques in Rashba ferromagnets. *Phys. Rev. B* **86,** 014416 (2012).
16. Wang, X. H. & Manchon, A. Diffusive spin dynamics in ferromagnetic thin films with a Rashba interaction. *Phys. Rev. Lett.* **108,** 117201 (2012).
17. Hals, K. M. D. & Brataas, A. Phenomenology of current-induced spin–orbit torques. *Phys. Rev. B* **88,** 085423 (2013).
18. Chernyshov, A. *et al.* Evidence for reversible control of magnetization in a ferromagnetic material by means of spin–orbit magnetic field. *Nature Phys.* **5,** 656–659 (2009).
19. Endo, M., Matsukura, F. & Ohno, H. Current induced effective magnetic field and magnetization reversal in uniaxial anisotropy (Ga,Mn)As. *Appl. Phys. Lett.* **97,** 222501 (2010).

20. Fang. D. *et al.* Spin–orbit-driven ferromagnetic resonance. *Nature Nanotech.* **6,** 413–417 (2011).
21. Kurebayashi, H. *et al.* An antidamping spin–orbit torque originating from the Berry curvature. *Nature Nanotech.* **9,** 211–217 (2014).
22. Miron, I. M. *et al.* Current-driven spin torque induced by the Rashba effect in a ferromagnetic metal layer. *Nature Mater.* **9,** 230–234 (2010).
23. Miron, I. M. *et al.* Fast current-induced domain-wall motion controlled by the Rashba effect. *Nature Mater.* **10,** 419–423 (2011).
24. Miron, I. M. *et al.* Perpendicular switching of a single ferromagnetic layer induced by in-plane current injection. *Nature* **476,** 189–193 (2011).
25. Garello, K. *et al.* Symmetry and magnitude of spin–orbit torques in ferromagnetic heterostructures. *Nature Nanotech.* **8,** 587–593 (2013).
26. Kim, J. *et al.* Layer thickness dependence of the current-induced effective field vector in Ta |CoFeB| MgO. *Nature Mater.* **12,** 240–245 (2013).
27. Fan, X. *et al.* Observation of the nonlocal spin-orbital effective field. *Nature Commun.* **4,** 1799 (2013).
28. Onsager, L. Reciprocal relations in irreversible processes. *Phys. Rev.* **37,** 405 (1931).
29. Tatara, G., Nakabayashi, N. & Lee, K. J. Spin motive force induced by Rashba interaction in the strong sd coupling regime. *Phys. Rev. B* **87,** 054403 (2013).
30. Jungwirth, T., Sinova, J., Masek, J., Kucera, J. & MacDonald, A. H. Theory of ferromagnetic (III,Mn)V semiconductors. *Rev. Mod. Phys.* **78,** 809 (2006).
31. Liu, L. Q., Moriyama, T., Ralph, D. C. & Buhrman, R. A. Spin–torque ferromagnetic resonance induced by the spin Hall effect. *Phys. Rev. Lett.* **106,** 036601 (2011).
32. Liu, X. Y. & Furdyna, J. K. Ferromagnetic resonance in $Ga_{1-x}Mn_xAs$ dilute magnetic semiconductors. *J. Phys. Condens. Matter* **18,** R245–R279 (2006).

Acknowledgements

A.F. acknowledges support from a Hitachi Research Fellowship and C.C. from a Junior Research Fellowship at Gonville and Caius College. V.N. acknowledges MSMT grant no. LM2011026.

Author contributions

K.H. and A.B. developed the theory and suggested the experiment. C.C. and A.J.F. developed the experimental technique and performed the experimental work. V.N. grew the materials. A.I. performed the nanofabrication. C.C., K.H., A.B. and A.F. wrote the manuscript. All authors discussed the results and commented on the paper.

Additional information

Supplementary information is available in the online version of the paper. Reprints and permissions information is available online at www.nature.com/reprints. Correspondence and requests for materials should be addressed to A.B.

Competing financial interests

The authors declare no competing financial interests.